Progressive alterations in polysomal architecture and activation of ribosome stalling relief factors in a mouse model of Huntington's disease

Eva Martin-Solana[a,1], Irene Diaz-Lopez[b], Yamina Mohamedi[c], Ivan Ventoso[d], Jose-Jesus Fernandez[a,c,e,*], Maria Rosario Fernandez-Fernandez[a,c,e,*]

[a] Centro Nacional de Biotecnología (CNB-CSIC). Campus UAM, Darwin 3, 28049 Madrid, Spain.

[b] MRC Laboratory of Molecular Biology. Cambridge Biomedical Campus, Cambridge, UK

[c] Instituto de Investigación Sanitaria del Principado de Asturias (ISPA). Av. Hospital Universitario s/n, 33011 Oviedo, Asturias, Spain.

[d] Centro de Biología Molecular "Severo Ochoa" (CSIC-UAM) and Departamento de Biología Molecular, Universidad Autónoma de Madrid (UAM). Madrid, Spain.

[e] Centro de Investigación en Nanomateriales y Nanotecnología (CINN-CSIC). Av. Vega 4-6, 33940 El Entrego, Asturias, Spain.

[1] Current address: Department of Psychiatry, University of Pittsburgh, Pittsburgh, PA, 15213, USA.

[*] **Corresponding authors:**

jj.fernandez@csic.es, **mr.fernandez@csic.es**

Individual email addresses:

E Martin-Solana: EVM43@pitt.edu

I Diaz-Lopez: idiaz@mrc-lmb.cam.ac.uk

Y Mohamedi: yamina.mohamedi@ispasturias.es

I Ventoso: iventoso@cbm.csic.es

JJ Fernandez: JJ.Fernandez@csic.es

MR Fernandez-Fernandez: MR.Fernandez@csic.es

Abstract

Given their highly polarized morphology and functional singularity, neurons require precise spatial and temporal control of protein synthesis. Alterations in protein translation have been implicated in the development and progression of a wide range of neurological and neurodegenerative disorders, including Huntington's disease (HD). In this study we examined the architecture of polysomes in their native brain context in striatal tissue from the zQ175 knock-in mouse model of HD. We performed 3D electron tomography of high-pressure frozen and freeze-substituted striatal tissue from HD models and corresponding controls at different ages. Electron tomography results revealed progressive remodelling towards a more compacted polysomal architecture in the mouse model, an effect that coincided with the emergence and progression of HD related symptoms. The aberrant polysomal architecture is compatible with ribosome stalling phenomena. In fact, we also detected in the zQ175 model an increase in the striatal expression of the stalling relief factor *EIF5A2* and an increase in the accumulation of eIF5A1, eIF5A2 and hypusinated eIF5A1, the active form of eIF5A1. Polysomal sedimentation gradients showed differences in the relative accumulation of 40S ribosomal subunits and in polysomal distribution in striatal samples of the zQ175 model. These findings indicate that changes in the architecture of the protein synthesis machinery may underlie translational alterations associated with HD, opening new avenues for understanding the progression of the disease.

57 **Keywords:**

58 Huntington's disease, 3D electron tomography, ribosome, polysome, ribosome
59 stalling, eIF5A

60 Introduction

61 Huntington's disease (HD) is a genetically inherited dominant
62 neurodegenerative disorder caused by expansion of a CAG repeat sequence in
63 the coding sequence of huntingtin protein (HTT) [1]. Symptoms manifest at
64 middle age (35-45 years) and life expectancy after disease onset is usually 15–
65 20 years. Initially, the disease primarily affects the corpus striatum, and
66 neurodegeneration selectively affects medium-sized spiny neurons (MSSNs),
67 which are GABAergic projection neurons [2, 3]. HD patients develop
68 progressive motor dysfunction, cognitive decline, and psychological alterations
69 [4, 5]. Although different pharmacological approaches are being explored, there
70 is no effective treatment for the disease [6, 7]. Recently, promising clinical trials
71 of therapies based on antisense oligonucleotides were halted in phase III, as
72 the potential benefits did not outweigh the risks [8].

73 The CAG repeat is polymorphic in normal chromosomes and is expanded in
74 HD-mutated chromosomes [9]. The number of repeats influences the age of
75 onset and disease severity. The repeat is located in exon 1 and encodes a
76 polyglutamine sequence (polyQ) that resides in the N-terminal region of the
77 protein. The polyQ sequence in HTT is followed by a proline rich domain (PRD)
78 that is also polymorphic in the human population [10]. HTT is a large 348-kDa
79 protein with a considerable degree of conservation from flies to mammals [10].

However, exon 1 is less evolutionarily conserved than other exons. Interestingly, the PRD is found only in mammals, suggesting recent evolution of the HTT protein [11]. In yeast systems the presence of the PRD reduces the toxicity of exon 1 constructs containing polyQ sequences in the pathological range [12], and also reduces the rate of polyQ aggregation *in vitro* [13–16]. Normal HTT function and the basis for the toxic effects of mutant HTT (mHTT) in the context of HD are still not fully understood [17].

As a consequence of their polarized organization and the particularities of synaptic activity, neurons require precise spatial and temporal control of protein translation, and are therefore particularly susceptible to alterations in the mechanisms controlling protein translation [18]. Dysregulation of cellular mechanisms involved in protein synthesis has been widely implicated in the development and progression of diverse neurological and neurodegenerative diseases [18–21]. Specifically, several studies have shown that mutations in proteins involved in resolving ribosome stalling induce motor dysfunction, neurodegeneration [22], and neuronal cell death in mice [23]. A growing body of evidence points to alterations in mHTT translation and in overall protein synthesis in the context of HD. Surprisingly, mRNAs containing expanded CAG repeats are translated more efficiently than those in the non-pathological range [24]. A higher number of CAG repeats favours the binding of a translation regulation complex containing MID1-PP2A. Consequently, the accumulation of mHTT protein is considerably greater than that of non-pathological HTT. These results reveal an interesting gain of function of the mutant protein at the mRNA level [24]. Several research groups have evaluated translation in the context of HD using the SUnSET method, with conflicting findings. The method is based

105 on the ability of puromycin to label newly synthesized peptides when
106 administrated at low doses. On the one hand, Creus-Muncunill *et al*. reported
107 an increase in puromycin incorporation into striatal cells in brain slices from the
108 R6/1 HD mouse model [25], suggesting that protein translation is increased and
109 that an overall increase in protein translation could constitute a novel
110 pathogenic mechanism in HD. Interestingly, proteomic characterization
111 revealed that the increase in translation specifically affected a set of proteins
112 involved in ribosomal and oxidative phosphorylation, while other proteins
113 implicated in neuronal structure and function were downregulated. On the other
114 hand, Joag *et al.* reported reduced incorporation of puromycin into *Drosophila*
115 cells overexpressing a fragment of HTT containing a 138 polyQ expansion [26].
116 These results were also reproduced in SYS5 and Neuro2a cells and suggest
117 that expression of a pathogenic mHTT fragment induces a deficit in protein
118 synthesis. Similarly, a recent study reported reduced incorporation of puromycin
119 in heterozygous and homozygous ST*Hdh* cell lines generated from a knock-in
120 mouse model containing 111 CAGs as compared with wild type (wt)
121 counterparts (7 CAGs), suggesting reduced protein synthesis in HD [27]. HTT
122 was proposed to promote ribosome stalling through binding to ribosomes, an
123 effect that is exacerbated by mHTT [27]. Interestingly, yeast cells expressing
124 fragments of pathogenic exon 1 show downregulation in the expression of
125 genes implicated in ribosome biogenesis and rRNA processing and metabolism
126 [28], and hence general repression of protein synthesis. The discrepant findings
127 described above may well be due to the different HD models used, or may be
128 representative of distinct disease scenarios. Overall, these results point to
129 dysregulation of protein synthesis in the presence of mHTT.

130 Electron tomography allows the study of the 3D subcellular architecture and the
131 organization of molecules in their native cellular or tissue environment with
132 nanometric resolution [29, 30]. It is based on the acquisition of images from a
133 sample at different tilt angles that are subsequently processed and combined to
134 yield a 3D reconstruction or tomogram [31]. Multiple studies have employed
135 electron tomography to investigate the spatial distribution and interaction of
136 ribosomes in their native cellular context in bacteria [32], isolated glioblastoma
137 cells [33], and HeLa cells [34], and more recently as a proof of principle in
138 tissue in *Caenorhabditis elegans* [35]. Rapid-freezing techniques are used to
139 ensure optimal structural preservation of cells and tissues for electron
140 tomography. Specifically, high-pressure freezing (HPF) is used to fully vitrify
141 bulk specimens (up to 200–400 μm thick) through synchronized pressurization
142 and cooling of the sample within milliseconds. Tissue samples can either be
143 processed for observation under cryogenic conditions [35] or freeze-substituted
144 to replace the frozen cellular water with organic solvents and embedded in
145 resins at low temperature to proceed with the analysis at room temperature
146 [30,36]. While fully cryogenic conditions are ideal to preserve the structure in
147 closest-to-native conditions and to achieve the maximum structural resolution,
148 these protocols are not yet used routinely for tissues [35]. Thus, HPF and FS is
149 currently the combination of choice for systematic comparative analysis of
150 ultrastructural tissue alterations in pathological conditions [36].

151 In the present study, we explored the architecture of neuronal polysomes in
152 their native brain context using 3D electron tomography of HPF/FS striatal
153 tissue obtained from the zQ175 knock-in HD mouse model [37]. We observed
154 progressive remodelling of polysomal architecture resulting in a densely packed

155 conformation compatible with ribosome stalling phenomena. Supporting this
156 hypothesis, we observed increased expression of the stalling release factor
157 *EIF5A2* and an increase in the accumulation of eIF5A1, eIF5A2 and
158 hypusinated eIF5A1 in HD model striatal samples. Polysomal sedimentation
159 gradients revealed a remarkable increase in the accumulation of free 40S
160 ribosomal subunits in striatal samples from HD mice and differences in the
161 distribution of polysomes. These changes in the architecture of the protein
162 synthesis machinery may constitute the basis of translational alterations
163 associated with HD.

164

165

166 # Materials and Methods

167 ## Animals

168 A stable colony of the zQ175 mice [37] was established using founders donated
169 by the Cure Huntington's Disease Initiative (CHDI) and obtained from Jackson
170 Laboratory Inc. The zQ175 line is a knock-in line bred on a C57BL/6J
171 background with an endogenous murine *HTT* gene containing a chimeric
172 human/mouse exon 1 with approximately 190 CAG repeats (B6.12951-
173 Htt<tm1Mfc<190JChdi). Heterozygous mice and controls were bred as a stable
174 colony in the animal facility of the Centro Nacional de Biotecnología, Madrid,
175 and provided with food and water *ad libitum*. All experiments complied with
176 Spanish and European legislation and Spanish National Research Council
177 (CSIC) ethics committee on animal experimentation.

178 ## Sample preparation based on HPF/FS for electron microscopy

179 Brain tissue samples were prepared for electron microscopy (EM) and
180 tomography following our protocols for optimal structural preservation based on
181 high-pressure freezing and freeze-substitution (HPF/FS), as previously
182 described [36]. In short, mouse brains were dissected immediately post-mortem
183 and 200-µm-thick sagittal slices were cut using a tissue slicer (Stoelting, Co.).
184 Striatal samples were promptly extracted, placed on a flat specimen carrier, and
185 frozen under high-pressure in a Leica EMPACT2 device. The samples were
186 further processed with freeze-substitution of frozen water to methanol and
187 embedded in Lowicryl resin HM20 with a Leica AFS2 EM FSP system. Sections
188 (250 nm) were obtained from the resin-embedded samples using a Leica

189 Ultracut EM-UC6 ultramicrotome, and placed on Quantifoil S7/2 grids.

190

191 **Electron microscopy**

192 A conventional JEOL JEM-1011 electron microscope (100 kV) was used to
193 screen the 250-nm-thick sections, check the integrity of the tissue samples, and
194 select areas of interest. An average of 5 EM grids per age/genotype were
195 observed. Control and zQ175 animals of 2, 8, 10, and 11 months of age were
196 analysed (2 months: 2 wt males, 1 heterozygous female; 8 months: 1 wt male, 1
197 heterozygous male; 10 months: 2 wt males, 1 heterozygous male; 11 months: 2
198 wt males, 2 heterozygous males). Cells compatible with striatal medium-sized
199 spiny neurons were selected based on morphological criteria [38] (Fig. S1) and
200 representative cytoplasmic areas with abundant ribosomes were selected for
201 subsequent 3D studies with ET.

202

203 **Electron tomography**

204 Tomographic data were acquired by taking series of images from the sections
205 while tilting them within a range of ±60° at 1° intervals around a single tilt-axis.
206 The tilt-series were acquired using a Thermo Fisher Scientific Talos Arctica
207 electron microscope (200 kV) equipped with a Falcon II electron direct detector
208 or using a FEI Tecnai G2 (200 kV) equipped with a CCD camera. The pixel size
209 at the specimen level was 0.37 nm and 0.59 nm, respectively. For processing,
210 visualization and analysis, images were rescaled with a binning factor of 4. Prior
211 to ET, grids were incubated in a solution of 10-nm diameter colloidal gold
212 (EM.BSA 10, Electron Microscopy Sciences, Hatfield, PA, USA) to facilitate

213 subsequent image alignment. An average of 10 cells were analysed per animal
214 and an average of 16 tomograms taken per animal.

215 Tilt-series alignment and calculation of the 3D tomograms were conducted
216 using IMOD standard software [39], applying standard protocols [31]. Images of
217 the tilt-series were mutually aligned using the colloidal gold beads as fiducial
218 markers. Tomograms were reconstructed with the standard method, weighted
219 back-projection (WBP), using a filter that simulates an iterative reconstruction
220 method (SIRT) [31].

221 **Computational analysis of the ribosomal pattern in tomograms**

222 To characterize the ribosomal pattern observed in the tomograms, we
223 developed computational procedures to (1) automatically identify ribosomes
224 and (2) examine how they are organized. The procedure for ribosome
225 identification is based on the Laplacian of Gaussian (LoG), a strategy
226 commonly used in the field of computer vision to detect 'blobs'. Here, we
227 extended this strategy to 3D in order to work with tomograms. Essentially, the
228 procedure applies Gaussian filtering, with a standard deviation related to the
229 size of the target 3D blob (i.e., the ribosome, around 25 nm in diameter) and,
230 afterwards, a Laplacian operator (i.e., second-order derivative) is applied to the
231 Gaussian-filtered tomogram. The peaks in the resulting LoG map correspond to
232 positions at which ribosomes are located in the tomogram. The final ribosome
233 positions are extracted using a segmentation operation based on thresholding
234 of the LoG map.

235

236 To analyse ribosomal organization based on the detected ribosome positions,

we implemented second-order spatial point pattern analysis techniques extended to 3D. Specifically, we used Ripley's K function [40], *K(r)*, which allows us to measure the expected number of ribosomes within a distance *r* from an arbitrary ribosome, normalized by the density of the ribosome distribution. This function can be mathematically expressed as follows:

$$K(r) = V \cdot \frac{\sum_{i=1}^{n} \sum_{j \neq i} e_i(r) \cdot I\left[d_{ij} \leq r\right]}{n^2}$$

where *V* is the volume of the tomogram, *n* denotes the number of ribosomes in the tomogram, d_{ij} represents the Euclidean distance from the ribosome *i* to *j*, *I[.]* is an indicator function that equals 1 if the distance d_{ij} is within the radius *r,* and otherwise equals 0. The term $e_i(r)$ is an edge-correction factor to properly weight the contribution of ribosomes with partial neighbourhood due to their proximity to the edge of the tomogram [40]. Ripley's K function is calculated at a range of distances *r*, with a recommended maximum value that should be lower than half of the shortest dimension of the sample domain [40, 41]. In this work, the spatial analysis was applied at distances ranging from 25 nm (i.e. ribosome diameter) to 100 nm.

Under the hypothesis of complete spatial randomness (CSR), the K function is equal to the volume of a sphere of radius *r*: $K_{CSR}(r) = 4/3 \cdot \pi \cdot r^3$. The ratio $K(r)/K_{CSR}(r)$ thus allows analysis of the ribosomal distribution pattern and its classification into the three main categories [42]: aggregation or clustering (if $K(r)/K_{CSR}(r) > 1$); regularity or dispersion (if $K(r)/K_{CSR}(r) < 1$); or random (if $K(r)/K_{CSR}(r) = 1$). Fig. S2 illustrates the calculation of Ripley's K function and the three main spatial distribution patterns.

Analysis of the ribosomal distribution was applied to selected tomograms from 10 and 11-month-old animals, acquired on a FEI Tecnai G2 microscope. The larger field of view of this microscope allowed acquisition of regions with an area up to 2.4 µm x 2.4 µm.

qRT-PCR

Striatal samples from 12-month-old mouse brains were used for gene expression analysis (8 heterozygous zQ175 animals: 4 females, 4 males and 8 corresponding matched wt controls: 4 females, 4 males). The following genes were analysed: *EIF5A1*, *EIF5A2*, *DHPS,* and *DOHH.* The primers used are described in (Table 1).

Table 1. Primers used for qRT-PCR of target genes of interest

Gene	ENSEMBL	Primer	Sequence 5'- 3'	Amplicon size
eIF5A1	ENSMUSG00000078812	Fw[a]	GGATGTCCCCAACATCAAAC	75 bp
		Rv[b]	TCCTGGAGCAGGGATAGGTA	
eIF5A2	ENSMUSG00000050192	Fw	GCAAAATCGTGGAGATGTCA	127 bp
		Rv	TCCATGTTGTGAGTAGAAGGACA	
DHPS	ENSMUSG00000060038	Fw	TACCTCGTGCAGCACAACA	102 bp
		Rv	GAACTCGCCAAGGTATGTGG	
DOHH	ENSMUSG00000078440	Fw	CCGGGCCCTGTTTACACT	60 bp
		Rv	CGGCTGATCCACGAGATAG	

[a]Fw: forward primer

[b]Rv: reverse primer

277 Reference genes were used for normalization of gene expression data (*GAPDH*,
278 *BACT*, *B2M*, *18S,* and *YWHAZ* (Table 2).

279 **Table 2. Primers used for amplification by qRT-PCR of reference genes for**
280 **normalization**

Gene	Primer	Sequence 5 '- 3'	Amplicon size
18S	Fw[a]	CTCAACACGGGAAACCTCAC	110 bp
	Rv[b]	CGCTCCACCAACTAAGAACG	
BACT	Fw	CTAAGGCCAACCGTGAAAAG	104 bp
	Rv	ACCAGAGGCATACAGGGACA	
B2M	Fw	TACATACGCCTGCAGAGTTAAGCA	76 bp
	Rv	TGATCACATGTCTCGATCCCAG	
GAPDH	Fw	CACCACCAACTGCTTAGCCC	76 bp
	Rv	TGTGGTCATGAGCCCTTCC	
YWHAZ	Fw	TTACTTGGCCGAGGTTGCT	60 bp
	Rv	TGCTGTGACTGGTCCACAAT	

281 [a]Fw: forward primer
282 [b]Rv: reverse primer
283

284 The suitability of reference genes for normalization of gene expression was
285 evaluated using Normfinder algorithm, which showed that *YWHAZ w*as the
286 most stable and accurate gene for normalization. Total RNA was isolated using
287 the Maxwell 16 LEV simply RNA tissue kit (Promega, #AS1280), and RNA
288 integrity was assessed using the Agilent 2100 Bioanalyzer. RIN values ranged
289 from 7 to 9.9, indicating a very high level of sample integrity. cDNA synthesis
290 was performed using the iScript cDNA Synthesis kit (Bio-Rad, #170-8891).
291 qRT-PCR was performed in triplicate on a CFX384 Real Time System C1000

292 Thermal Cycler (Bio-rad) using Sso Fast EvaGreen Supermix (Bio-Rad, #172-
293 5204). Reactions included a non-template control and primer efficiency curves
294 were generated. ValidPrime kit (TATAA Biocenter, #A105S10) was used as
295 control for genomic background (gDNA). The contribution of gDNA to qPCR
296 signal was less than 6.5% in all cases. A melting curve from 60°C to 95°C
297 (0.5°C/seg) was included at the end of the program to verify the specificity of
298 the PCRs. Data processing was carried out using GenEx v5.4.4 (MultiD
299 Analysis AB, Gothenburg, Sweden). The $2^{-\Delta(\Delta Cq)}$ method was used to
300 calculate the relative fold change in gene expression of samples normalized to
301 *YWHAZ* gene expression [43].

302 **Cell culture and transfection**

303 HEK293T cells were cultured in DMEM medium (Sigma, #D6429)
304 supplemented with 10% inactivated foetal bovine serum, non-essential amino
305 acids (1:100, Sigma, #M7145), 0.5 μg/ml amphotericin B (Fungizone™)
306 (Gibco™, #15290018), penicillin-streptomycin (1:100, Sigma, #P4333), and 50
307 μg/ml gentamycin (Sigma, #G1397). Cells were cultured at 37ºC in a 5% CO_2
308 atmosphere.

309 pEGFP-Q23 and pEGFP-Q74 plasmids were a gift from David Rubinsztein
310 (Addgene plasmid # 40261 and 40262) [44]. These express a GFP protein
311 fused to the sequence encoded by part of human *HTT* exon1. Fusion proteins
312 contain either a non-pathological polyQ repeat (23Q) or a polyQ repeat in the
313 pathological range (74Q). These plasmids were co-transfected with pCMV-NP
314 (a plasmid expressing the influenza virus nucleoprotein) as a transfection
315 control [45].

316 The day before transfection 6×10^5 cells were plated per well in a M6 plate
317 (Falcon, # 353046) to obtain 70-80% confluence. For actual transfection,
318 plasmids were diluted in a solution containing 250 mM $CaCl_2$ to achieve a final
319 amount of 1 or 3 μg per well (final volume per well: 3 ml) for *HTT* plasmids and
320 2 μg for pCMV-NP. The DNA/$CaCl_2$ solution was mixed for 1 min with an equal
321 volume of filtered HBS buffer (50 mM HEPES pH 7.05, 1.5 mM Na_2HPO_4, 140
322 mM NaCl). Cells were harvested in the culture medium after the corresponding
323 period of incubation and centrifuged at 210 *g* for 5 min at 4ºC. The pellet was
324 then washed with PBS1x and centrifuged as before. The pellet was frozen and
325 stored at -80ºC. Cell lysis was achieved by thermal shock (3 cycles of 15 min at
326 RT+ 30 min at -80ºC) in a buffer containing 50 mM Tris-HCl pH 7.4 and 150 mM
327 NaCl. The lysate was centrifuged at 16,100 *g* for 10 min at 4ºC and the
328 supernatant used for Western-blot (WB) analysis as described below. Before
329 recovery of the cells, the plates were observed under a Leica DMI6000B
330 microscope at 10x magnification for the detection of GFP-fused proteins.

331 **Polysome sedimentation gradients**

332 Polysome profiles were generated as previously described [46–48], with some
333 modifications. Briefly, the striatum was dissected from brain and immediately
334 frozen in liquid nitrogen. Samples from mice of the same genotype were pooled
335 to overcome the limitation of the low sample weight (4 mice per genotype: 2
336 males, 2 females). Frozen samples were ground with a mortar and pestle under
337 liquid nitrogen and homogenized in ice-cold polysome extraction buffer (20 mM
338 HEPES pH 7.4, 150 mM KCl, 5 mM $MgCl_2$, 0.5 mM DTT, 1% Triton X-100, 200
339 μg/ml cycloheximide [CHX], heparin 20 μg/ml, and 40 U/ml RNase inhibitor

340 [New England Biolabs, Cat. no. M0307S]) using a potter homogenizer (10–12
341 strokes). After three passages through a 23G needle, the homogenates were
342 centrifuged at 2000 *g* for 5 min at 4ºC. The supernatants were subsequently
343 centrifuged twice at 16,100 *g* for 10 min at 4ºC. The final supernatants (600 μl)
344 were loaded onto 10–50% continuous sucrose density gradients in polysome
345 buffer (20 mM HEPES pH 7.4, 150 mM KCl, 5 mM $MgCl_2$) (Gradient Master™,
346 BioComp) and centrifuged in an SW40Ti swing-out rotor (Beckman Coulter) at
347 250,000 *g* for 2 h at 4ºC. Fractions (1 ml) were collected using a density
348 gradient fractionation system (ISCO) with continuous monitoring of absorbance
349 at 254 nm.

350 Polysomal sedimentation gradients of transfected cells were performed as
351 previously described [49], with some modifications. Briefly, 24 h post
352 transfection, HEK293T cells were treated with 100 µg/ml CHX for 3 min at 37°C.
353 Cells were then washed 3 times with cold CHX (100 µg/ml) in PBS (1x),
354 harvested with residual CHX/PBS and centrifuged at 1000 *g* for 5 min at 4°C.
355 The cell pellet was washed with ice-cold CHX/PBS, centrifuged at 1000 *g* for 5
356 min at 4°C and resuspended in 500 µl of polysome extraction buffer (100 µg/ml
357 CHX without heparin). The cell lysate was mixed through a 23G needle and
358 incubated on ice for 10 min (vortexing every 2-3 min). The homogenates were
359 centrifuged at 2000 *g* for 5 min at 4ºC and subsequently centrifuged twice at
360 16,100 *g* for 10 min at 4ºC. The final supernatants (400 µl) were loaded onto a
361 10–50% continuous sucrose density gradient (Gradient Station™, BioComp)
362 and centrifuged in an SW40Ti swing-out rotor at 250,000 *g* for 2 h at 4ºC.
363 Fractions (1 ml) were collected manually.

364 **Western-blot analysis**

365 Bulk striatal samples were processed for WB as described previously [50]:
366 seven 15 month old heterozygous animals (2 females, 5 males) and seven
367 corresponding wt controls were used (4 females, 3 males). Samples (25-30
368 micrograms total protein) were loaded onto 4-20% (Bio-Rad, #4561096) mini-
369 protean TGX precast gels and run in Tris-glycine/SDS running buffer (Bio-Rad,
370 #1610732). Proteins were transferred to nitrocellulose membranes (BioRad,
371 1620112). For normalization total protein content was quantified by using
372 Revert™ 700 Total Protein Stain (926-11021, LI-COR). Membranes were
373 incubated with the following antibodies: mouse monoclonal raised against
374 eIF5A1 (SAB1402762, Merck), rabbit polyclonal raised against eIF5A2 (17069-
375 1-AP, Proteintech) and rabbit polyclonal anti-hypusine (ABS1064-I, Merck).

376 Fractions from sucrose gradients were loaded onto NuPAGE 12% Bis-Tris gels
377 (Invitrogen, NP0343) and run in MES running buffer (Invitrogen, NP0002) and
378 transferred as described above. Membranes were incubated with the following
379 primary antibodies: rabbit polyclonal anti-RPS6 (Elabscience, E-AB-32813),
380 anti-RPL7 (Elabscience, E-AB-32805), and anti-hypusine (Creative Biolabs,
381 PABL-202). For accurate quantitative comparisons membranes were first
382 incubated with anti-RPS6 antibody. After completing the WB, membranes were
383 consecutively incubated with anti-RPL7 antibody. For this reason, the residual
384 signal of anti-RPS6 antibody is visible in images of the RPL7 signal.

385 Samples from transfected HEK293T cells were processed as shown above and
386 membranes were incubated consecutively with anti-GFP (Genetex
387 #GTX113617) and anti-NP [45].

388 The secondary antibodies used were either IRDye 680RD (925-68071, Li-Cor)
389 and IRDye 800CW (925-32210, Li-Cor) (for bulk striatal samples analysis and
390 eIF5A1/eIF5A2 antibody characterization) or AffiniPure Goat anti-rabbit IgG
391 (H+L) (Jackson ImmunoResearch, 111-035-003) for the rest of WBs. IRDye
392 antibodies were used at 1:2500 and AffiniPure ones at 1:1000 dilutions. The
393 peroxidase reaction for AffiniPure antibodies was developed with Clarity™
394 Western ECL substrate (Bio-Rad, 1705061). Imaging was performed using
395 either an Odyssey Fc imaging system (Li-Cor) (quantified using Image
396 StudioTM software) or a Molecular ChemiDoc^{TM} Touch Imaging System (Bio-
397 Rad) (quantified using Image Lab 6.0.1 software).

398 **Statistical analysis**

399 Statistical analyses were performed using GrapPad Prism 8. Normal distribution
400 of the data was assessed using the Shapiro-Wilk test. A two-tailed unpaired
401 Student t-test was used to compare normal distributed data (after assessing the
402 equality of variances using Levene's test and/or Welch's correction). The level
403 of significance was set at $p<0.05$. All data are presented as mean ± SD.

404

405 # Results

406 **Ribosomal/polysomal organization is altered in medium-sized spiny**
407 **neurons in the striatum of zQ175 mice**

408 HD involves the selective degeneration of striatal MSSNs. Therefore, we
409 examined the architecture of the protein synthesis machinery in its native
410 cellular context, using electron tomography to identify and characterize
411 alterations in these neurons.

412 Brain tissue samples from HD animal models (heterozygous zQ175) at different
413 ages (2, 8, 10, and 11 months) and the corresponding controls were prepared
414 with HPF/FS for electron microscopy and tomography, as described in the
415 Materials and Methods. This preparation protocol ensures optimal structural
416 preservation of tissue samples. Conventional bidimensional (2D) electron
417 microscopy of 250 nm-thick sections was used to confirm sample integrity and
418 select areas of interest. Representative cytoplasmic areas were selected from
419 the soma of cells compatible with striatal MSSNs where ribosomal and
420 polysomal crowding was identified and examined by electron tomography to
421 determine 3D volumes.

422

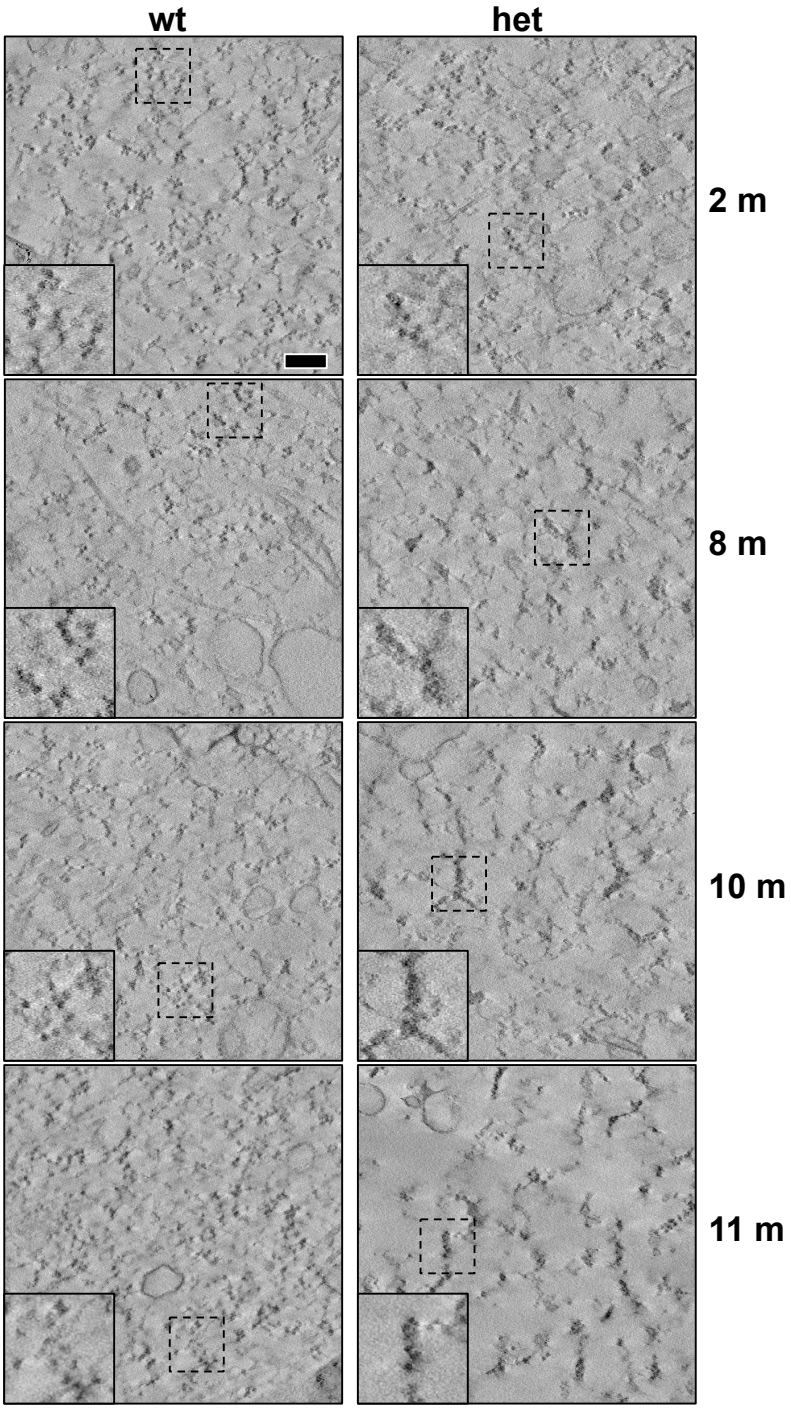

Figure 1. Progressive alterations in ribosomal/polysomal architecture in HD observed with ET. Slices of tomograms from wt (left) and heterozygous (het) zQ175 mice (right). From top to bottom, images correspond to mice aged 2, 8, 10, and 11 months. Insets are magnified views of dashed-line boxes. Scale bar: 200 nm.

429 Fig. S3 and S4 show representative EM images and slices of 3D volumes
430 obtained from a wt control and a zQ175 heterozygous mice at advanced age
431 (11 months). In wt samples ribosomes are abundant, are continuously
432 distributed across the entire cytoplasm, and form polysomal clusters in which
433 individual ribosomes can be clearly identified. By contrast, ribosomal density is
434 reduced in the zQ175 model and the polysomes form sparse clusters of tightly-
435 coupled ribosomes with large areas of empty cytoplasmic space between the
436 clusters. Fig. 1 shows representative tomographic slices from animals at
437 different ages: the distinctive pattern in HD mice becomes more pronounced
438 with age. Together, these results indicate that remodelling of polysomal
439 architecture in HD begins at ages (8 months) when some of the relevant
440 phenotypes of this model (diminished rotarod performance, striatal atrophy) [37]
441 become apparent. Moreover, these alterations in polysomal architecture show a
442 clear age-related progression.

443 To conduct an objective quantitative analysis, we developed a methodology for
444 automated identification of ribosomes in tomograms followed by a second-order
445 spatial analysis using Ripley's K function, as described in the Materials and
446 Methods section. Fig. S3D and S4D depict the detection of ribosomes in
447 respective tomograms from wt controls and zQ175 mice. These images show
448 that the cytoplasm in wt animals is densely populated with ribosomes whereas
449 in zQ175 mice the ribosomes are organized in groups.

450 Spatial analysis was applied to the ribosome positions in selected tomograms of
451 different neurons from 10 and 11-month-old animals (Figs. 1 and S5). Ripley's
452 K-function *K(r)* estimates the number of ribosomes around an arbitrary

453 ribosome within a distance *r*, normalized by ribosomal density. The plots in Fig.
454 2 depict Ripley's K-function relative to a random distribution ($K(r)/K_{CSR}(r)$, see
455 Materials and Methods). Thus, a unit value indicates a random distribution
456 whereas values >1 imply clustering. The functions show that the ribosomes are
457 significantly more clustered in the heterozygous HD model ($K(r)/K_{CSR}(r)$ much
458 higher than 1) than in wt controls, especially within shorter distances (up to 50
459 nm). Additionally, differences in the clustering at 10 and 11-months in the HD
460 model confirm that the phenotype is progressively evolving with age. The wt
461 phenotype also shows some ribosome clustering, though much less
462 pronounced than in the HD model. This is consistent with the fact that
463 ribosomes form polysomes to ensure efficient translation. We also calculated
464 ribosomal density (number of detected ribosomes per volume unit), which was
465 higher in wt controls than the HD model (5163 vs. 2686 ribosomes/μm^3,
466 analysis combining the 10 and 11-month old animals).

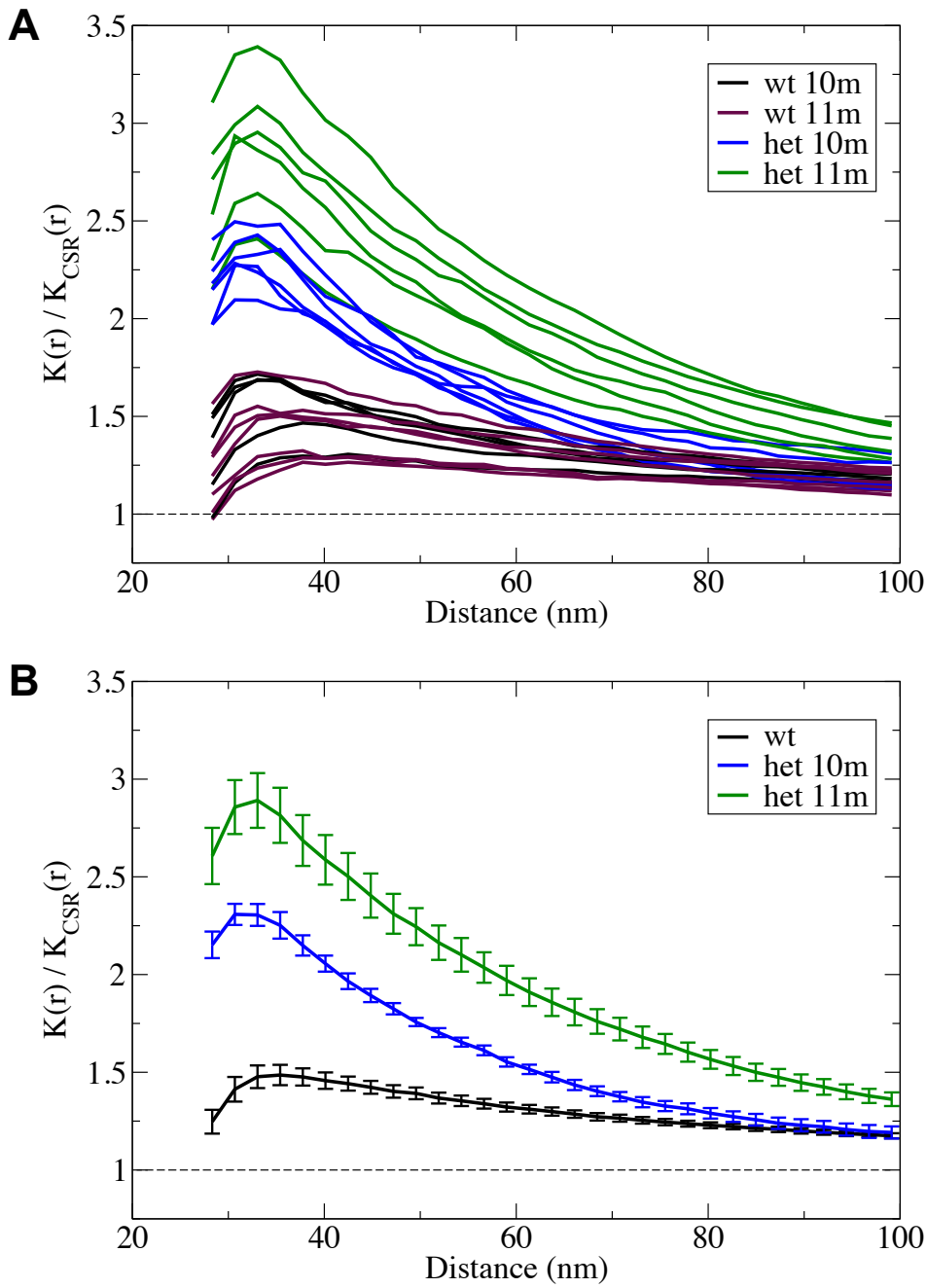

Figure 2. Second-order spatial pattern analysis based on Ripley's K function. Ripley's K-function relative to a random distribution, $K(r)/K_{CSR}(r)$ as a function of the distance calculated for tomograms from different neurons in heterozygous zQ175 and wt mice at ages of 10 and 11 months (A). The plot in (B) depicts mean values and the standard error from the curves of the zQ175 mice at the different ages and also for all wt mice. These Ripley's K-function plots represent the expected number of ribosomes within a distance r around a random ribosome *(K(r)),* relative to the expected value in a random distribution ($K_{CSR}(r)$). Values >1 indicate clustering.

477 **eIF5A stalling relief factors are activated in the striatum of heterozygous**
478 **zQ175 mice**

479 The polysomal architecture phenotype of the zQ175 model is reminiscent of
480 ribosome stalling phenomena. It is well established that the presence of
481 consecutive prolines in a polypeptide, as occurs in the PRD region of HTT,
482 induces ribosome stalling. Proline is neither a good donor nor a good acceptor
483 during peptide bond formation, as the reactive amine is embedded in the cyclic
484 lateral chain, thus reducing its nucleophilicity [51–53]. eIF5A and its homologue
485 in bacteria, EF-P, have been shown to participate in stimulating peptide bond
486 formation between consecutive prolines, thereby releasing ribosome stalling
487 [54–56].

488 eIF5A is encoded by two distinct genes, giving rise to two different homologous
489 proteins: eIF5A1 and eIF5A2 [57]. While eIF5A1 is widely expressed in all
490 tissues, eIF5A2 is weakly expressed in the majority of tissues with the exception
491 of certain areas of the brain and testis, where higher levels are detected [58].
492 eIF5A proteins are the only known proteins containing the amino acid hypusine,
493 formed by a posttranslational modification of lysine. The role of eIF5A in
494 releasing ribosome stalling is dependent on hypusine [53, 59, 60]. Formation of
495 hypusine involves two enzymatic reactions [60, 61]: deoxyhypusine synthase
496 (DHS) produces deoxyhypusine, which is then hydroxylated by deoxyhypusine
497 hydroxylase (DOHH) to produce hypusine. We investigated whether activation
498 of the eIF5A pathway may be specifically induced in zQ175 mice. Using qRT-
499 PCR, we analysed the expression of eIF5A factors and related genes in the
500 striatum of 12-month old zQ175 mice and corresponding wt controls. As shown
501 in Fig. 3A, we observed no significant difference in the expression of genes

encoding eIF5A1, DHPS, or DOHH, and a significant increase in the expression of *EIF5A2* in the striatum of zQ175 heterozygous animals. Overexpression of *EIF5A2* could reflect a response to stalling in HD conditions. It is important to note that the analysis of bulk striatal samples could conceal differences that may be specific to MSSNs.

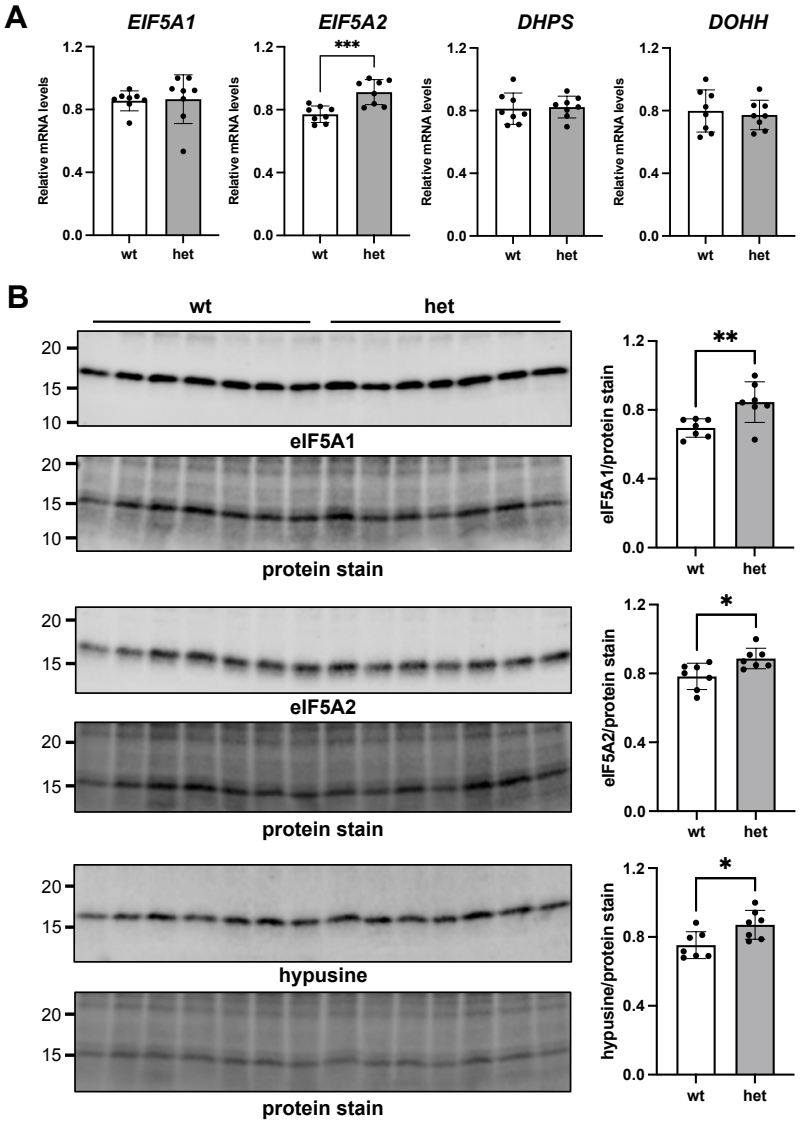

Figure 3. eIF5A stalling relief factors are activated in the striatum of heterozygous zQ175 mice. (A) Relative accumulation of *EIF5A1*, *EIF5A2*, *DHPS* and *DOHH* mRNA in the striatum of heterozygous zQ175 mice and wt controls analysed by qRT-PCR. Data are normalized to expression levels of the reference gene *YWHAZ*. For each independent gene the highest value after

513 normalization to *YWHAZ* was set to 1 to facilitate comparisons. Data followed a
514 normal distribution (Shapiro-Wilk test) with the exception of *EIF5A1*. No
515 significant difference between groups was observed for *EIF5A1, DHPS,* or
516 *DOHH* gene expression (p=0.2786, 0.8130, and 0.6642, respectively). *EIF5A2*
517 expression was significantly increased in heterozygous zQ175 mice versus
518 controls (p=0.0009). Data are presented as the mean ±SD (n=8). **(B)** Western-
519 blot analysis of the accumulation of eIF5A1, eIF5A2 and hypusinated eIF5A
520 factor in the striatum of 15-month-old heterozygous zQ175 mice and wt controls.
521 In the eIF5A2 blot the shadow band below the eIF5A2 corresponds to the
522 antibody cross-reaction with eIF5A1 (see Fig. S6). Total protein in each lane
523 was quantified by staining with Revert™ 700 Total Protein Stain (926-11021, LI-
524 COR) for normalization of loading. The panel in the figure shows only the area
525 in the molecular weight range of the proteins of interest. Graphs on the right
526 show the quantification of relative accumulation. In all cases data followed a
527 normal distribution. We detected a significant increase in the accumulation of
528 eIF5A1 (p=0.0095), eIF5A2 (p=0.0149) and hypusinated eIF5A1 (p=0.0181) in
529 the heterozygous animals. Data are presented as the mean ±SD (n=7).

530

531 We next examined the accumulation of eIF5A1, eIF5A2 and hypusinated eIF5A
532 forms in striatal samples by WB. eIF5A1 and eIF5A2 have an 84% identity at
533 the amino acid level, consequently many antibodies raised against one of them
534 cross-react with the other. To unequivocally distinguish both isoforms we
535 evaluated the specificity of the antibodies used in this work against recombinant
536 eIF5A1 and eIF5A2 expressed in bacteria (Fig. S6).

537 We observed a significant increase in the relative accumulation of eIF5A1,
538 eIF5A2 and the hypusine containing form of eIF5A1 in the striatum of
539 heterozygous zQ175 mice versus corresponding wt controls at 15 months of
540 age (Fig. 3B). We were not able to detect in this WB a band corresponding to
541 the hypusine containing form of eIF5A2 (Fig. S6B).

542 Next, we investigated whether there is any differential recruitment of the active
543 (hypusinated) form of eIF5A1 to ribosomes. We optimized a protocol to prepare
544 polysomal sedimentation gradients: given the low weight of the mouse striatum

545 the protocol was performed using a pool of samples from 4 animals. Fig. 4A
546 shows the profiles obtained for the wt and heterozygous zQ175 pools. The
547 peaks corresponding to 40S (small subunit), 60S (large subunit), 80S
548 (monosome), and polysomes are clearly identifiable in the profiles. Analysis of
549 the fractions by WB (Fig. 4B) confirmed the expected distribution of ribosomal
550 proteins corresponding to small and large subunits (RPS6 and RPL7),
551 respectively. For both wt and heterozygous zQ175 mice, most of the
552 hypusinated eIF5A (>80%) was detected in fractions 1 and 2, which do not
553 contain ribosomal subunits. Thus, most of the active stalling relief factor is not
554 associated to ribosomes. This result could be consistent with a transient
555 interaction of the factor with the 60S subunit [62], or could be indicative of
556 functions of the eIF5A factor other than facilitating elongation in polyproline-
557 induced stalling, as previously proposed [59, 63–65].

558 The profiles of polysomal sedimentation gradients (Fig. 4A) were largely similar
559 for wt and heterozygous zQ175 mice: we observed no remarkable differences
560 in the polysomal area that could correspond to the polysomal compaction
561 phenotype observed by ET. However, the profiles obtained suggest a higher
562 40S:80S ratio in heterozygous zQ175 versus wt mice. Analysis of fractions by
563 WB (Fig. 4B) showed that the ratio of RPS6 accumulation in fraction 3 (40S)
564 versus fraction 5 (80S) is higher in the heterozygous zQ175 (1.01) than in the
565 wt (0.77), thereby confirming an increased accumulation of free 40S ribosomal
566 subunit in the striatum of heterozygous zQ175 animals. Interestingly, the WB
567 analysis (Fig. 4B) also showed a different distribution of ribosomal proteins in
568 the polysomal area. In the heterozygous zQ175 gradient we observed a
569 maximum peak in fraction 11 (for both RPS6 and RPL7), while in the wt

570 gradient the proteins were more widely distributed across surrounding fractions,
571 with equivalent levels detected in fractions 10 and 11. The relevance of this
572 differential distribution of polysomes and its relation to the architectural
573 phenotype detected by ET remains to be determined.

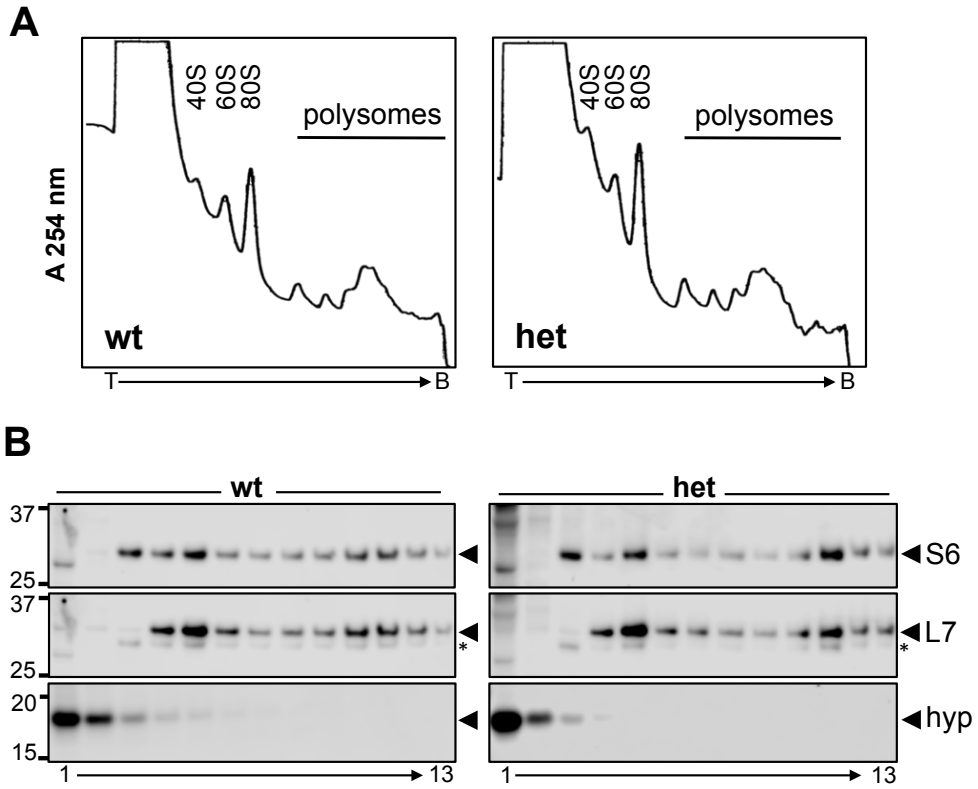

574

575 **Figure 4. Polysomal sedimentation gradients generated from striatal**
576 **samples from 9-month-old wt and heterozygous zQ175 mice. (A)** Profiles
577 obtained by continuous monitoring of absorbance at 254 nm. Peaks
578 corresponding to 40S, 60S, 80S, and polysomes are identifiable. T indicates the
579 top and B the bottom of the gradient. **(B)** Accumulation of RPS6 (S6), RPL7
580 (L7) and hypusinated eIF5A factor in gradient fractions. Fraction 1 corresponds
581 to the top and fraction 13 to the bottom of the gradient. Most hypusinated eIF5A
582 (>80%) accumulates in the first two fractions that do not contain ribosomal
583 subunits (soluble fractions). Asterisks indicate the residual signal of RPS6.

584

585 **The expanded CAG repeat does not have a negative effect on protein**
586 **accumulation**

587 Next, we explored whether differences in the ribosomal and polysomal
588 organization observed in the striatum of zQ175 mice models are a direct
589 consequence of mHTT expression. We transfected HEK293T cells with
590 plasmids to overexpress GFP protein fused to the sequence encoded by part of
591 the *HTT* exon1 containing either 23 (pEGFP-Q23) or 74 (pEGFP-Q74) CAG
592 repeats, which represent non-pathological and pathological conditions,
593 respectively [44]. Different plasmid concentrations were used (1 μg and 3 μg
594 per well). As a control of transfection, cells were co-transfected with the pNP
595 plasmid (pCMV-NP) [45]. Results in Fig. 5A and 5B show that for both plasmids
596 higher concentrations are associated with greater accumulation of the fusion
597 proteins. Interestingly, at both plasmid concentrations accumulation of the GFP-
598 Q74 fusion protein was greater than that of GFP-Q23 (with a significant effect
599 observed for 3 μg). A similar effect was previously reported [24] in transfection
600 experiments using mouse embryonic fibroblasts and plasmids that express 17Q
601 and 49Q tracks in the context of a wider N-terminal HTT fragment (first 500
602 amino acids). Those authors observed no differences in the expression of
603 mRNAs encoding Q17 and Q49. They also showed that increasing the number
604 of CAG repeats favours binding of the MID1-PP2A-containing translation
605 regulation complex, thus supporting the view that differences in translation
606 efficiency underlie the protein accumulation effect. Our results confirm that this
607 effect is highly dependent on the CAG sequence coding for the polyQ, as the
608 plasmids we used contain the CAG repeat in the context of a partial and short

609 exon 1 sequence (polyQ is flanked in the N- and C-terminus by 10 and 17 aa

610 encoded by exon 1, respectively).

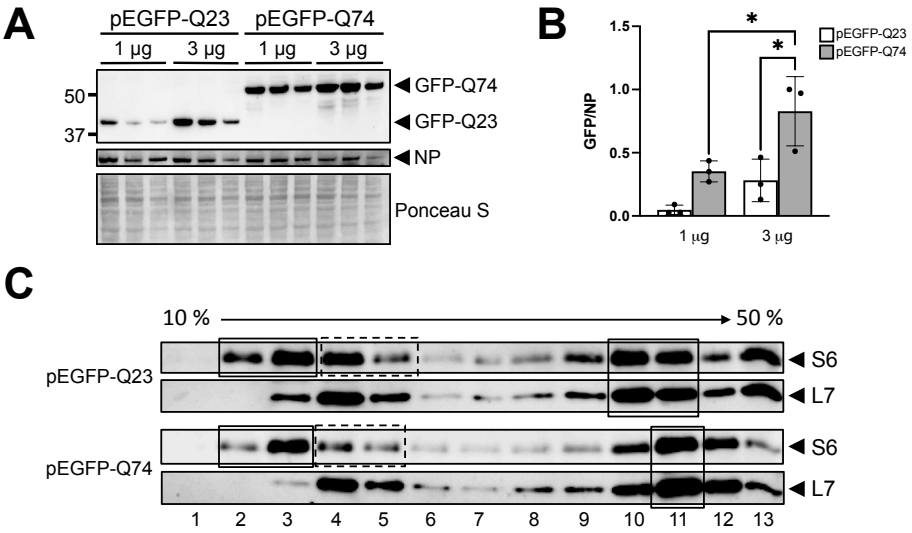

611

612 **Figure 5. Transfection of HEK293T cells with plasmids expressing a GFP**
613 **fusion protein containing part of the exon1 *HTT* coding sequence**
614 **including 23Q or 74Q. (A)** Accumulation of fusion proteins GFP-Q23 and GFP-
615 Q74 18 hours post-transfection. Middle panel shows NP protein accumulation
616 as a transfection control. The bottom panel shows the Ponceau S staining.
617 Samples were run in triplicate. **(B)** Quantification of the relative accumulation of
618 GFP-Q23 and GFP-Q74 for the different transfection conditions shown in **A**.
619 Mean ± SD values are shown. Increased accumulation of GFP-Q74 was
620 observed at both plasmid concentrations: significant at 3 µg (p=0.0422) but not
621 at 1 µg (p=0.1000). For both plasmids an increase in the amount of transfected
622 plasmid was associated with increased accumulation of the fusion protein (not
623 significant for GFP-Q23 (p=0.1000) but for GFP-Q74 (p=0.0453)). The pEGFP-
624 Q23 1 µg dataset showed a non-normal distribution, all other groups had a
625 normal distribution. **C)** WB analysis of fractions from polysomal sedimentation
626 gradients obtained from HEK293T cells transfected with either pEFGP-Q23 or
627 pEGFP-Q74. Cells were recovered 24 hours post-transfection and the
628 percentage of transfection was 20-25%. Solid boxes on the left highlight the
629 accumulation of RPS6 (small ribosomal subunit) in the fractions of the gradient
630 likely corresponding to 40S subunit and the dashed boxes those corresponding
631 to 80S subunit. The 40S/80S ratio of RPS6 accumulation is 1.4 for GFP-Q23
632 and 2.8 for GFP Q74, confirming that overexpression of GFP-74Q fusion protein
633 is associated with increased percentage of free 40S subunits. Boxes on the
634 right highlight the differential accumulation of polysomes in the mid polysomal
635 area. Membranes were first incubated with anti-RPS6 and then reincubated

636 with anti-RPL7.

637 **Overexpression of constructs containing CAG repeats in the pathological**
638 **range is sufficient to induce increased accumulation of free 40S ribosomal**
639 **subunits**

640 We next explored whether differences in the polysome sedimentation gradients
641 observed in striatal samples from heterozygous zQ175 mice are a direct effect
642 of mHTT expression. We performed polysomal sedimentation gradient analyses
643 using pEFGFP-Q23- and pEGFP-Q74-transfected cells 24 hours post-
644 transfection. This was done applying the modifications described in the
645 Materials and Methods, and therefore there is a different distribution of the
646 ribosomal species in the fractions of the gradient as compared to gradients
647 performed with striatal samples. As shown in Fig. 5C the differential
648 accumulation of ribosomal proteins, RPS6 and RPL7, indicates that RPS6
649 accumulation in fractions 2 and 3 is representative of 40S subunit while that in
650 fractions 4 and 5 is representative of 80S. The gradients from cells
651 overexpressing GFP-Q74 (pathogenic range) revealed changes similar to those
652 observed in striatal samples from heterozygous zQ175 mice. Specifically, we
653 could determine that GFP-Q74 overexpression induces increased accumulation
654 of free 40S subunit (Fig. 5C). Additionally, differences observed in the
655 polysomal area mirrored those detected in gradients of striatal samples. While
656 GFP-Q74-overexpressing cells showed maximum accumulation around fraction
657 11, ribosomal proteins were more widely distributed across surrounding
658 fractions in GFP-Q23-overexpressing cells.

659

660 ## Discussion

661 One of the most intriguing characteristics of HD is its slowly progressive nature.
662 While the mutant protein is expressed throughout life, symptoms only begin to
663 manifest at middle age (35-45 years of age), and subsequent life expectancy is
664 15-20 years. Subtle alterations at the cellular level have been proposed to
665 accumulate overtime, only exerting detrimental effects at later stages [10]. Our
666 electron tomography results indicate progressive disturbance of neuronal
667 polysomal architecture in the striatum of the zQ175 mouse model of HD. In this
668 model, motor coordination phenotypes (measured by rotarod performance) and
669 striatal atrophy become evident from 8 months of age [37]. Interestingly, 8
670 months was the earliest time point at which rearrangements of polysome
671 structure were evident in our study. This coincidence and the importance of
672 protein synthesis for cellular homeostasis, suggest that the polysomal
673 alterations described here may be relevant to the development of HD-related
674 phenotypes and may reflect disease progression. The protein synthesis
675 disturbances associated with HD [25–27] have led some authors to propose
676 that translational dysfunction contributes to the pathogenesis of HD and that
677 new therapies targeting protein synthesis could help alleviate disease
678 symptoms [26]. Our results further underscore the role of translational
679 dysfunction in HD and point to alterations in the architecture of the protein
680 synthesis machinery as a starting point for translational dysfunction.

681 Studies using gene-specific deletion approaches have enabled the identification
682 of yeast strains in which mHTT toxicity is suppressed [28]. Interestingly, mHTT
683 overexpression in these strains results in increased expression of the stalling

684 relief factor *EIF5A2*. The increased *EIF5A2* expression that we detected in the
685 striatum of heterozygous zQ175 animals could represent a cellular response to
686 mHTT toxicity. Increased *EIF5A2* expression, increased accumulation of
687 eIF5A1, eIF5A2 and hypusinated eIF5A1 together with progressive compaction
688 of polysomes support a scenario of ribosome stalling induced by mHTT.

689 eIF5A factors are mainly involved in releasing the ribosome stalling induced by
690 the translation of consecutive prolines [54–56]. Interestingly, the polyQ
691 sequence in HTT is followed by a PRD with abundant consecutive prolines. This
692 PRD is present in both wt and mutant HTT, begging the question why stalling
693 induced by the translation of the PRD is only evident in heterozygous animals.
694 An interesting study reported that the dependence of stalling release on eIF5A
695 factors correlates with the translation initiation rate of each particular mRNA [66].
696 Thus, when initiation rates are low, translation through polyproline sequences
697 resumes without impeding the progression of upstream ribosomes, even in the
698 absence of eIF5A factors. However, transcripts with a high initiation rate will
699 often engage simultaneously with several ribosomes, which are likely to stall
700 when translating the polyproline sequence and become dependent on the
701 action of eIF5A factors. This is particularly relevant in the context of the findings
702 of Krauß *et al.,* who showed that a higher number of CAG repeats favours
703 binding of the MID1-PP2A-containing translation regulation complex, resulting
704 in more efficient translation [24]. Together, these findings suggest that mHTT
705 mRNA may be more sensitive to the effect of polyproline-mediated stalling
706 because it is more efficiently translated and therefore more dependent on the
707 action of eIF5A relief factors.

708 We describe excess accumulation of free 40S subunits in the striatum of the
709 heterozygous zQ175 mouse model of HD. The stability and accumulation of
710 small and large ribosomal subunits are coupled as part of a process that may
711 have evolved to ensure adequate translational performance. An excess of 40S
712 subunits could lead to the formation of translation initiation complexes that
713 cannot be converted to fully translating 80S ribosomes and consequently
714 sequester mRNAs, resulting in general disruption of protein synthesis [67].

715 Conclusions

716 Our findings underscore the role of translational dysfunction in HD and point to
717 alterations in the architecture of the protein synthesis machinery in the basis of
718 such dysfunction. Further studies are needed to understand the underlying
719 mechanisms by which mutations associated to HD induce these alterations.

720

721 Abbreviations

722 2D: Bi-dimensional

723 3D: Three-dimensional

724 CCD: Charge-coupled device

725 CSR: Complete spatial randomness

726 DHS: Deoxyhypusine synthase

727 DOHH: Deoxyhypusine hydroxylase

728 EIF5A: Eukaryotic Translation Initiation Factor 5A

729 EM: Electron microscopy

730 ET: Electron tomography

731 FS: Freeze-substitution

732 GABA: Gamma-aminobutyric acid

733 HD: Huntington's disease

734 HPF: High-pressure freezing

735 HTT: Huntingtin protein

736 LoG: Laplacian of Gaussian

737 mHTT: Mutant huntingtin protein

738 MSSNs: Medium-sized spiny neurons

739 polyQ: polyglutamine

740 PRD: Proline rich domain

741 qRT-PCR: Quantitative reverse transcription polymerase chain reaction

742 RPS6: 40S ribosomal protein S6

743 RPL7: 60S ribosomal protein L7

744 SD: Standard deviation

745 SIRT: Simultaneous iterative reconstruction technique

746 SUnSET: Surface sensing of translation

747 WB: Western blot

748 WBP: Weighted backprojection

749 wt: Wild type

750

751 # Declarations

752 **Ethical approval and consent to participate**

753 All experiments complied with Spanish and European legislation and Spanish
754 National Research Council (CSIC) ethics committee on animal experimentation.

755

756 **Consent for publication**

757 All authors have approved of the contents of this manuscript and provided
758 consent for publication.

759

760 **Availability of data and materials**

761 The data of this study are available from the corresponding authors on
762 reasonable request.

763

764 **Competing interests**

765 The authors declare no competing interests.

766

Funding

This work was mainly supported by a grant from Fundación Ramón Areces (CIVP18A3892). The Spanish AEI (SAF2017-84565-R, TED2021-132020B-I00, PID2022-139071NB-I00) and the Huntington's disease Society of America (HDSA) (Human Biology project 2022 awarded to MRFF) provided additional funding.

Authors' contributions

(CRediT: https://onlinelibrary.wiley.com/doi/epdf/10.1002/leap.1210)

EMS: Investigation, Validation, Formal Analysis, Methodology, Writing - Original draft .

IDL: Investigation, Resources, Writing - Review & Editing.

YM: Investigation

IV: Investigation, Resources, Writing - Review & Editing.

JJF: Conceptualization, Methodology, Software, Investigation, Formal Analysis, Writing - Original draft, Funding Acquisition.

MRFF: Conceptualization, Methodology, Investigation, Validation, Formal Analysis, Writing - Original draft, Funding Acquisition.

All authors read and approved the final manuscript.

Acknowledgements

We thank Pablo Sola Alarcón for valuable technical assistance. We would also like to thank Eber Martínez and all staff at the Animal Facility of the Centro Nacional de Biotecnología (CNB-CSIC, Madrid) for their work over the years. qPCR experiments were conducted at the Genomics and NGS Core Facility at the Centro de Biología Molecular Severo Ochoa, which is part of the CEI UAM+CSIC, Madrid. HPF and FS experiments together with the observation of brain sections were performed in the Electron Microscopy Facility at the CNB-CSIC. The acquisition of tilt series for tomography was performed in the Cryoelectron Microscopy Facility at CNB-CSIC. We are profoundly grateful to the Fundación Ramón Areces for the grant CIVP18A3892 that made this work possible, and to AEI (SAF2017-84565-R, TED2021-132020B-I00, PID2022-139071NB-I00) and Huntington's disease Society of America (HDSA) (Human Biology project 2022) for additional funding. We would also like to thank the Cure Huntington's disease initiative (CHDI) for providing the initial founders of the zQ175 colony within the context of a previous project.

805 # References

806 1. Bates GP (2005) History of genetic disease: the molecular genetics of
807 Huntington disease - a history. Nat Rev Genet 6:766–773.
808 https://doi.org/10.1038/nrg1686

809 2. Albin RL, Reiner A, Anderson KD, et al (1992) Preferential loss of striato-
810 external pallidal projection neurons in presymptomatic Huntington's disease.
811 Ann Neurol 31:425–430. https://doi.org/10.1002/ana.410310412

812 3. Vonsattel J-P, Myers RH, Stevens TJ, et al (1985) Neuropathological
813 Classification of Huntington's Disease: J Neuropathol Exp Neurol 44:559–577.
814 https://doi.org/10.1097/00005072-198511000-00003

815 4. Bates GP, Dorsey R, Gusella JF, et al (2015) Huntington disease. Nat
816 Rev Dis Primer 1:15005. https://doi.org/10.1038/nrdp.2015.5

817 5. Ross CA, Tabrizi SJ (2011) Huntington's disease: from molecular
818 pathogenesis to clinical treatment. Lancet Neurol 10:83–98.
819 https://doi.org/10.1016/S1474-4422(10)70245-3

820 6. Caron NS, Dorsey ER, Hayden MR (2018) Therapeutic approaches to
821 Huntington disease: from the bench to the clinic. Nat Rev Drug Discov 17:729–
822 750. https://doi.org/10.1038/nrd.2018.133

823 7. Tabrizi SJ, Ghosh R, Leavitt BR (2019) Huntingtin Lowering Strategies
824 for Disease Modification in Huntington's Disease. Neuron 101:801–819.
825 https://doi.org/10.1016/j.neuron.2019.01.039

826 8. Kwon D (2021) Failure of genetic therapies for Huntington's devastates
827 community. Nature 593:180–180. https://doi.org/10.1038/d41586-021-01177-7

828 9. Macdonald M (1993) A novel gene containing a trinucleotide repeat that
829 is expanded and unstable on Huntington's disease chromosomes. Cell 72:971–
830 983. https://doi.org/10.1016/0092-8674(93)90585-E

831 10. Saudou F, Humbert S (2016) The Biology of Huntingtin. Neuron 89:910–
832 926. https://doi.org/10.1016/j.neuron.2016.02.003

833 11. Tartari M, Gissi C, Lo Sardo V, et al (2008) Phylogenetic comparison of
834 huntingtin homologues reveals the appearance of a primitive polyQ in sea
835 urchin. Mol Biol Evol 25:330–338. https://doi.org/10.1093/molbev/msm258

836 12. Duennwald ML, Jagadish S, Muchowski PJ, Lindquist S (2006) Flanking
837 sequences profoundly alter polyglutamine toxicity in yeast. Proc Natl Acad Sci
838 U S A 103:11045–11050. https://doi.org/10.1073/pnas.0604547103

839 13. Bhattacharyya A, Thakur AK, Chellgren VM, et al (2006) Oligoproline
840 effects on polyglutamine conformation and aggregation. J Mol Biol 355:524–535.
841 https://doi.org/10.1016/j.jmb.2005.10.053

842 14. Dehay B, Bertolotti A (2006) Critical role of the proline-rich region in

843 Huntingtin for aggregation and cytotoxicity in yeast. J Biol Chem 281:35608–
844 35615. https://doi.org/10.1074/jbc.M605558200

845 15. Yang J, Hao X, Cao X, et al (2016) Spatial sequestration and
846 detoxification of Huntingtin by the ribosome quality control complex. eLife
847 5:e11792. https://doi.org/10.7554/eLife.11792

848 16. Meriin AB, Zhang X, Alexandrov IM, et al (2007) Endocytosis machinery
849 is involved in aggregation of proteins with expanded polyglutamine domains.
850 FASEB J Off Publ Fed Am Soc Exp Biol 21:1915–1925.
851 https://doi.org/10.1096/fj.06-6878com

852 17. Nowogrodzki A (2018) Huntington's disease: 4 big questions. Nature
853 557:S48. https://doi.org/10.1038/d41586-018-05180-3

854 18. Kapur M, Monaghan CE, Ackerman SL (2017) Regulation of mRNA
855 Translation in Neurons—A Matter of Life and Death. Neuron 96:616–637.
856 https://doi.org/10.1016/j.neuron.2017.09.057

857 19. Darnell JC (2014) Ribosome rescue and neurodegeneration. Science
858 345:378–379. https://doi.org/10.1126/science.1257193

859 20. Gao F-B, Richter JD, Cleveland DW (2017) Rethinking Unconventional
860 Translation in Neurodegeneration. Cell 171:994–1000.
861 https://doi.org/10.1016/j.cell.2017.10.042

862 21. Kapur M, Ackerman SL (2018) mRNA Translation Gone Awry:
863 Translation Fidelity and Neurological Disease. Trends Genet 34:218–231.
864 https://doi.org/10.1016/j.tig.2017.12.007

865 22. Chu J, Hong NA, Masuda CA, et al (2009) A mouse forward genetics
866 screen identifies LISTERIN as an E3 ubiquitin ligase involved in
867 neurodegeneration. Proc Natl Acad Sci 106:2097–2103.
868 https://doi.org/10.1073/pnas.0812819106

869 23. Ishimura R, Nagy G, Dotu I, et al (2014) Ribosome stalling induced by
870 mutation of a CNS-specific tRNA causes neurodegeneration. Science 345:455–
871 459. https://doi.org/10.1126/science.1249749

872 24. Krauß S, Griesche N, Jastrzebska E, et al (2013) Translation of HTT
873 mRNA with expanded CAG repeats is regulated by the MID1–PP2A protein
874 complex. Nat Commun 4:1511. https://doi.org/10.1038/ncomms2514

875 25. Creus-Muncunill J, Badillos-Rodríguez R, Garcia-Forn M, et al (2019)
876 Increased translation as a novel pathogenic mechanism in Huntington's disease.
877 Brain 142:3158–3175. https://doi.org/10.1093/brain/awz230

878 26. Joag H, Ghatpande V, Desai M, et al (2020) A role of cellular translation
879 regulation associated with toxic Huntingtin protein. Cell Mol Life Sci 77:3657–
880 3670. https://doi.org/10.1007/s00018-019-03392-y

881 27. Eshraghi M, Karunadharma PP, Blin J, et al (2021) Mutant Huntingtin
882 stalls ribosomes and represses protein synthesis in a cellular model of
883 Huntington disease. Nat Commun 12:1461. https://doi.org/10.1038/s41467-021-

884 21637-y

885 28. Tauber E, Miller-Fleming L, Mason RP, et al (2011) Functional Gene
886 Expression Profiling in Yeast Implicates Translational Dysfunction in Mutant
887 Huntingtin Toxicity. J Biol Chem 286:410–419.
888 https://doi.org/10.1074/jbc.M110.101527

889 29. Frank J (2006) Electron Tomography. Springer New York, New York, NY

890 30. He W, Fernández J-J (2010) Electron Tomography. In: John Wiley &
891 Sons, Ltd (ed) Encyclopedia of Life Sciences. John Wiley & Sons, Ltd,
892 Chichester, UK, p a0021877

893 31. Fernandez J-J (2012) Computational methods for electron tomography.
894 Micron 43:1010–1030. https://doi.org/10.1016/j.micron.2012.05.003

895 32. Brandt F, Etchells SA, Ortiz JO, et al (2009) The Native 3D Organization
896 of Bacterial Polysomes. Cell 136:261–271.
897 https://doi.org/10.1016/j.cell.2008.11.016

898 33. Brandt F, Carlson L-A, Hartl FU, et al (2010) The Three-Dimensional
899 Organization of Polyribosomes in Intact Human Cells. Mol Cell 39:560–569.
900 https://doi.org/10.1016/j.molcel.2010.08.003

901 34. Mahamid J, Pfeffer S, Schaffer M, et al (2016) Visualizing the molecular
902 sociology at the HeLa cell nuclear periphery. Science 351:969–972.
903 https://doi.org/10.1126/science.aad8857

904 35. Schaffer M, Pfeffer S, Mahamid J, et al (2019) A cryo-FIB lift-out
905 technique enables molecular-resolution cryo-ET within native Caenorhabditis
906 elegans tissue. Nat Methods 16:757–762. https://doi.org/10.1038/s41592-019-
907 0497-5

908 36. Fernandez-Fernandez MR, Ruiz-Garcia D, Martin-Solana E, et al (2016)
909 3D electron tomography of brain tissue unveils distinct Golgi structures that
910 sequester cytoplasmic contents in neurons. J Cell Sci jcs.188060.
911 https://doi.org/10.1242/jcs.188060

912 37. Menalled LB, Kudwa AE, Miller S, et al (2012) Comprehensive
913 behavioral and molecular characterization of a new knock-in mouse model of
914 Huntington's disease: zQ175. PloS One 7:e49838.
915 https://doi.org/10.1371/journal.pone.0049838

916 38. Matamales M, Bertran-Gonzalez J, Salomon L, et al (2009) Striatal
917 Medium-Sized Spiny Neurons: Identification by Nuclear Staining and Study of
918 Neuronal Subpopulations in BAC Transgenic Mice. PLoS ONE 4:e4770.
919 https://doi.org/10.1371/journal.pone.0004770

920 39. Kremer JR, Mastronarde DN, McIntosh JR (1996) Computer
921 Visualization of Three-Dimensional Image Data Using IMOD. J Struct Biol
922 116:71–76. https://doi.org/10.1006/jsbi.1996.0013

923 40. Ripley BD (1988) Statistical Inference for Spatial Processes, 1st ed.
924 Cambridge University Press

925 41. Baddeley AJ, Moyeed RA, Howard CV, Boyde A (1993) Analysis of a
926 Three-Dimensional Point Pattern with Replication. Appl Stat 42:641.
927 https://doi.org/10.2307/2986181

928 42. Diggle PJ (2013) Statistical Analysis of Spatial and Spatio-Temporal
929 Point Patterns, 0 ed. Chapman and Hall/CRC

930 43. Livak KJ, Schmittgen TD (2001) Analysis of Relative Gene Expression
931 Data Using Real-Time Quantitative PCR and the 2−ΔΔCT Method. Methods
932 25:402–408. https://doi.org/10.1006/meth.2001.1262

933 44. Narain Y, Wyttenbach A, Rankin J, et al (1999) A molecular investigation
934 of true dominance in Huntington's disease. J Med Genet 36:739–746.
935 https://doi.org/10.1136/jmg.36.10.739

936 45. Coloma R, Valpuesta JM, Arranz R, et al (2009) The Structure of a
937 Biologically Active Influenza Virus Ribonucleoprotein Complex. PLoS Pathog
938 5:e1000491. https://doi.org/10.1371/journal.ppat.1000491

939 46. Heiman M, Schaefer A, Gong S, et al (2008) A Translational Profiling
940 Approach for the Molecular Characterization of CNS Cell Types. Cell 135:738–
941 748. https://doi.org/10.1016/j.cell.2008.10.028

942 47. Nielsen H (2011) RNA: methods and protocols. Humana Press, New
943 York

944 48. Díaz-López I, Toribio R, Berlanga JJ, Ventoso I (2019) An mRNA-binding
945 channel in the ES6S region of the translation 48S-PIC promotes RNA
946 unwinding and scanning. eLife 8:e48246. https://doi.org/10.7554/eLife.48246

947 49. Pringle ES, McCormick C, Cheng Z (2019) Polysome Profiling Analysis
948 of mRNA and Associated Proteins Engaged in Translation. Curr Protoc Mol Biol
949 125:e79. https://doi.org/10.1002/cpmb.79

950 50. Fernandez-Fernandez MR, Ferrer I, Lucas JJ (2011) Impaired ATF6α
951 processing, decreased Rheb and neuronal cell cycle re-entry in Huntington's
952 disease. Neurobiol Dis 41:23–32. https://doi.org/10.1016/j.nbd.2010.08.014

953 51. Wohlgemuth I, Brenner S, Beringer M, Rodnina MV (2008) Modulation of
954 the Rate of Peptidyl Transfer on the Ribosome by the Nature of Substrates. J
955 Biol Chem 283:32229–32235. https://doi.org/10.1074/jbc.M805316200

956 52. Pavlov MY, Watts RE, Tan Z, et al (2009) Slow peptide bond formation
957 by proline and other N-alkylamino acids in translation. Proc Natl Acad Sci
958 106:50–54. https://doi.org/10.1073/pnas.0809211106

959 53. Melnikov S, Mailliot J, Rigger L, et al (2016) Molecular insights into
960 protein synthesis with proline residues. EMBO Rep 17:1776–1784.
961 https://doi.org/10.15252/embr.201642943

962 54. Doerfel LK, Wohlgemuth I, Kothe C, et al (2013) EF-P Is Essential for
963 Rapid Synthesis of Proteins Containing Consecutive Proline Residues. Science
964 339:85–88. https://doi.org/10.1126/science.1229017

965 55. Gutierrez E, Shin B-S, Woolstenhulme CJ, et al (2013) eIF5A Promotes
966 Translation of Polyproline Motifs. Mol Cell 51:35–45.
967 https://doi.org/10.1016/j.molcel.2013.04.021

968 56. Ude S, Lassak J, Starosta AL, et al (2013) Translation Elongation Factor
969 EF-P Alleviates Ribosome Stalling at Polyproline Stretches. Science 339:82–85.
970 https://doi.org/10.1126/science.1228985

971 57. Wu G-Q, Xu Y-M, Lau ATY (2020) Recent insights into eukaryotic
972 translation initiation factors 5A1 and 5A2 and their roles in human health and
973 disease. Cancer Cell Int 20:142. https://doi.org/10.1186/s12935-020-01226-7

974 58. Jenkins ZA, Hååg PG, Johansson HE (2001) Human EIF5A2 on
975 Chromosome 3q25–q27 Is a Phylogenetically Conserved Vertebrate Variant of
976 Eukaryotic Translation Initiation Factor 5A with Tissue-Specific Expression.
977 Genomics 71:101–109. https://doi.org/10.1006/geno.2000.6418

978 59. Saini P, Eyler DE, Green R, Dever TE (2009) Hypusine-containing
979 protein eIF5A promotes translation elongation. Nature 459:118–121.
980 https://doi.org/10.1038/nature08034

981 60. Schmidt C, Becker T, Heuer A, et al (2016) Structure of the
982 hypusinylated eukaryotic translation factor eIF-5A bound to the ribosome.
983 Nucleic Acids Res 44:1944–1951. https://doi.org/10.1093/nar/gkv1517

984 61. Park MH, Cooper HL, Folk JE (1981) Identification of hypusine, an
985 unusual amino acid, in a protein from human lymphocytes and of spermidine as
986 its biosynthetic precursor. Proc Natl Acad Sci 78:2869–2873.
987 https://doi.org/10.1073/pnas.78.5.2869

988 62. Rossi D, Barbosa NM, Galvão FC, et al (2016) Evidence for a Negative
989 Cooperativity between eIF5A and eEF2 on Binding to the Ribosome. PLOS
990 ONE 11:e0154205. https://doi.org/10.1371/journal.pone.0154205

991 63. Schuller AP, Green R (2018) Roadblocks and resolutions in eukaryotic
992 translation. Nat Rev Mol Cell Biol 19:526–541. https://doi.org/10.1038/s41580-
993 018-0011-4

994 64. Schuller AP, Wu CC-C, Dever TE, et al (2017) eIF5A Functions Globally
995 in Translation Elongation and Termination. Mol Cell 66:194-205.e5.
996 https://doi.org/10.1016/j.molcel.2017.03.003

997 65. Pelechano V, Alepuz P (2017) eIF5A facilitates translation termination
998 globally and promotes the elongation of many non polyproline-specific tripeptide
999 sequences. Nucleic Acids Res 45:7326–7338.
1000 https://doi.org/10.1093/nar/gkx479

1001 66. Hersch SJ, Elgamal S, Katz A, et al (2014) Translation Initiation Rate
1002 Determines the Impact of Ribosome Stalling on Bacterial Protein Synthesis. J
1003 Biol Chem 289:28160–28171. https://doi.org/10.1074/jbc.M114.593277

1004 67. Gregory B, Rahman N, Bommakanti A, et al (2019) The small and large
1005 ribosomal subunits depend on each other for stability and accumulation. Life Sci
1006 Alliance 2:e201800150. https://doi.org/10.26508/lsa.201800150

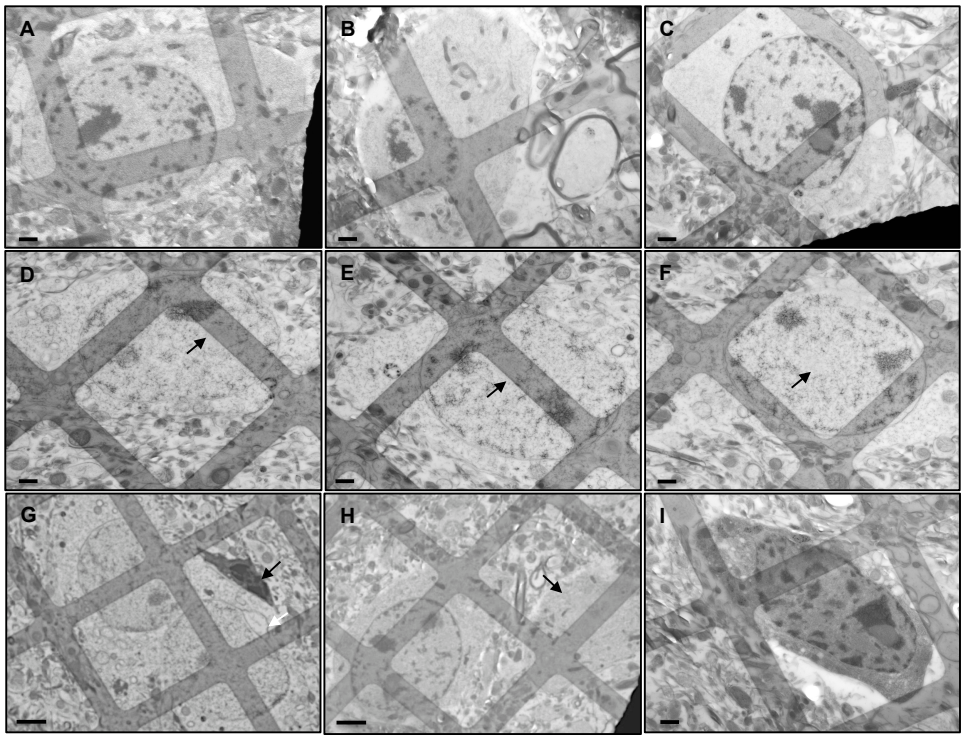

Supplementary Figure S1. Representative EM images of striatal cells from 250-nm-thick sections of brain tissue. (A-F) Cells compatible with medium-sized spiny neurons (MSSN) based on morphological criteria in wt control **(A-C)** and heterozygous zQ175 **(D-F)** mice aged 11 months. In the HD model, these cells appear paler, an effect evident in the chromatin, nucleus and cytoplasm. In addition, nuclear inclusions are identifiable in the HD model (arrows in D-F). **(G)** A cell, likely microglia, with nucleus and cytoplasm that are highly dense (black arrow) is observed near two pale cells compatible with MSSNs. One of these MSSNs contains a nuclear bleb (white arrow), which are often found in HD neurons and are indicative of neurodegeneration. **(H)** A putative MSSN and, on the right, an area of cytoplasm from another cell (arrow) with a similar appearance but not showing the nucleus. **(I)** A cell from a control animal, with size and morphology compatible with a MSSN, with highly dense nucleus and cytoplasm (signs of cell death). Scale bars: 1 µm (A-F, I), 2 µm (G-H).

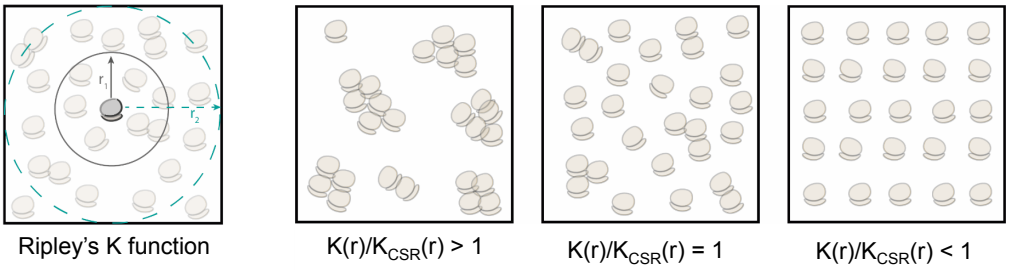

Supplementary Figure S2. Ripley's K function and spatial distribution patterns. Left: Ripley's K function is calculated at a range of distances *r* and measures the expected number of ribosomes within the distance *r* from an arbitrary ribosome, normalized by the density of the ribosome distribution. In this study, the K function has been implemented in 3D, though for simplicity the sketch depicts 2D. Right: Three main spatial distribution patterns can be identified when comparing the actual K function with the expected value under complete spatial randomness (K_{CSR}): clustering ($K(r)/K_{CSR}(r) > 1$); randomness ($K(r)/K_{CSR}(r) = 1$); and regularity or dispersion ($K(r)/K_{CSR}(r) < 1$).

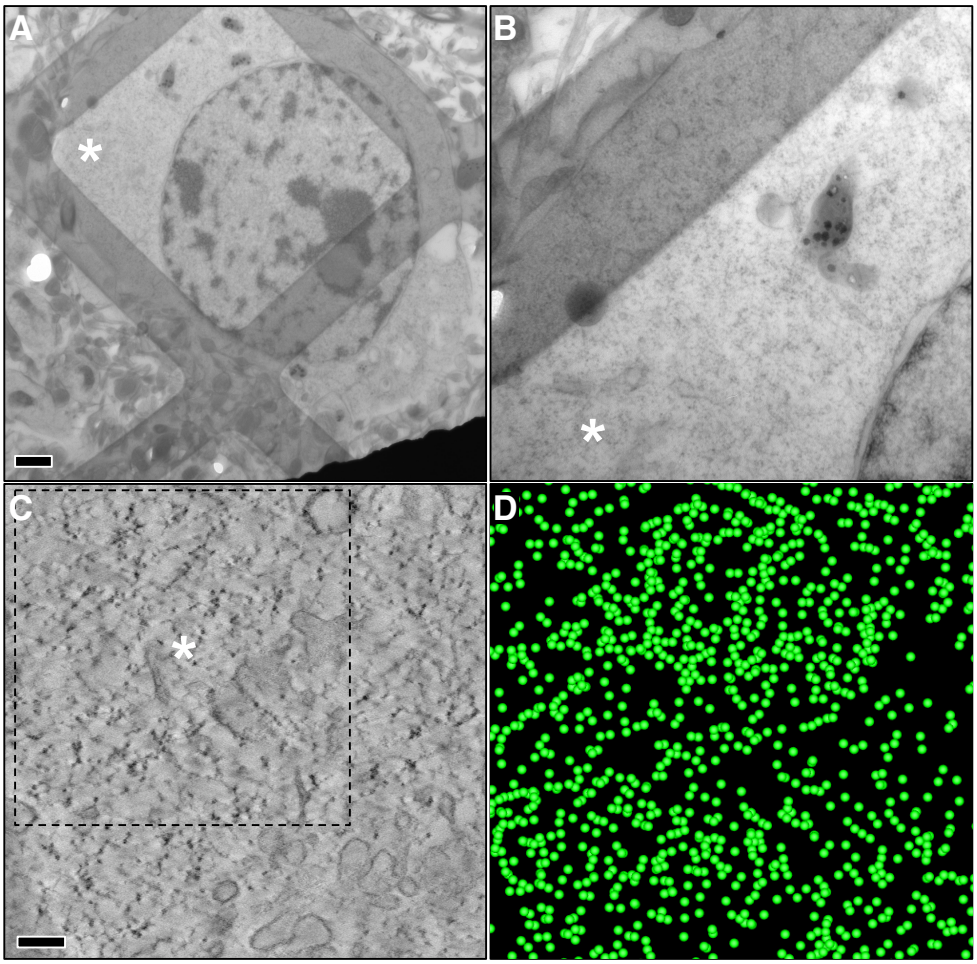

Supplementary Figure S3. Electron tomography of a striatal neuron from a 250 nm thick section of brain tissue from an 11-month-old wild-type mouse. (A) Image from conventional 2D electron microscopy, showing the nucleus of the neuron and cytoplasm. Scale bar: 1 µm. **(B)** Magnified view from the area marked by the asterisk in **A**. **(C)** Tomogram slice computed from a tilt-series acquired at the position marked with the asterisk in **B**. The individual ribosomes are clearly identifiable as black dots in the spotty cytoplasm. The cytoplasm is crowded by numerous ribosomes, and polysomal clusters are also observed. Scale bar: 200 nm. **(D)** 3D visualization of the ribosomes detected using our automated procedure based on Laplacian of Gaussian (LoG) and represented by green spheres. These ribosomes correspond to the area outlined with a dashed line in **C**.

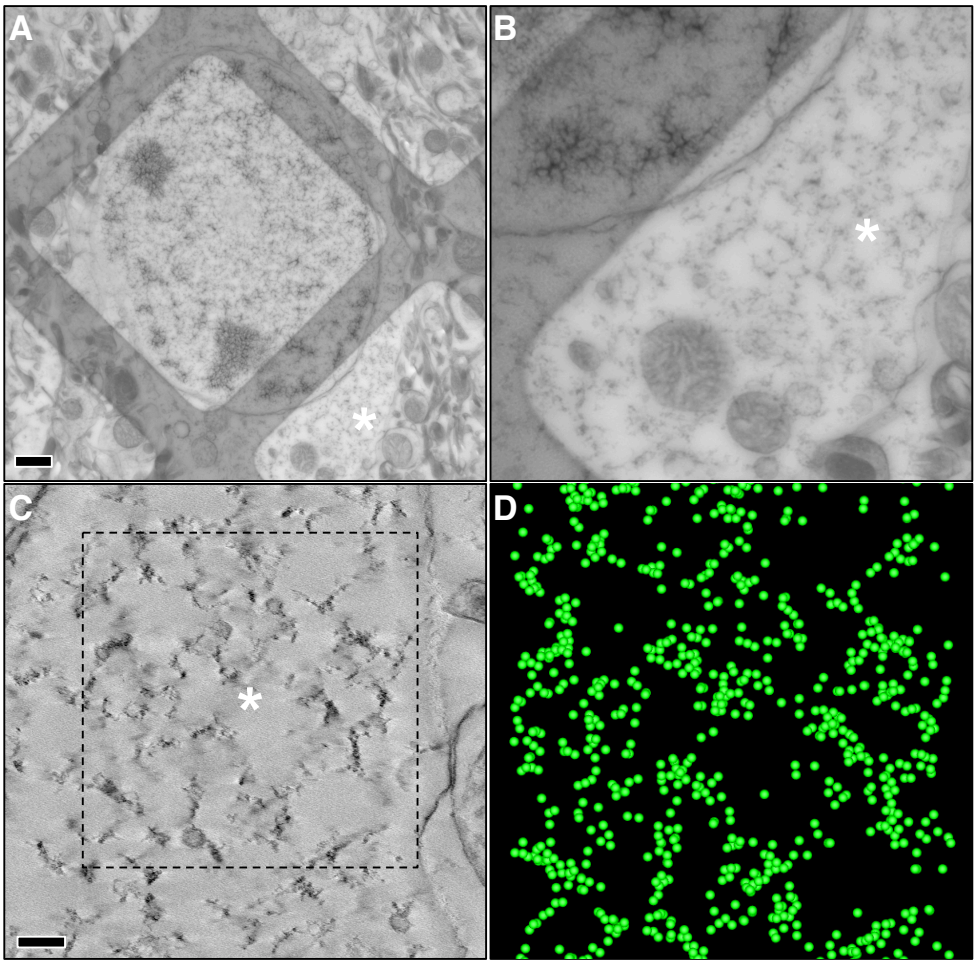

1049
1050 **Supplementary Figure S4. Electron tomography of a striatal neuron from a**
1051 **250-nm-thick section of brain tissue from an 11-month-old heterozygous**
1052 **zQ175 mouse. (A-D)** Interpretation of the panels as described in Figure S3. In
1053 this case, few individual ribosomes are observed in the tomogram (C). Instead,
1054 tightly-coupled clusters of ribosomes are evident, and there is substantial empty
1055 cytoplasmic space among the clusters.

1056

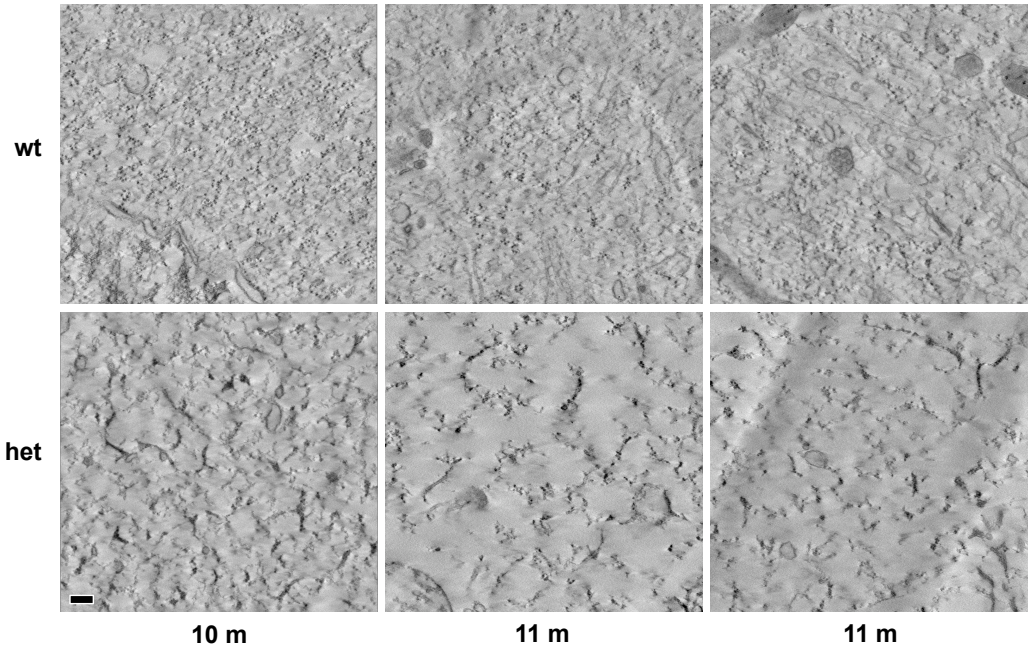

Figure S5.

1057
1058 **Supplementary Figure S5. Representative slices of tomograms from 10**
1059 **and 11-month-old wild-type control (top) and heterozygous zQ175**
1060 **(bottom) mice.** Scale bar: 200 nm.

1061

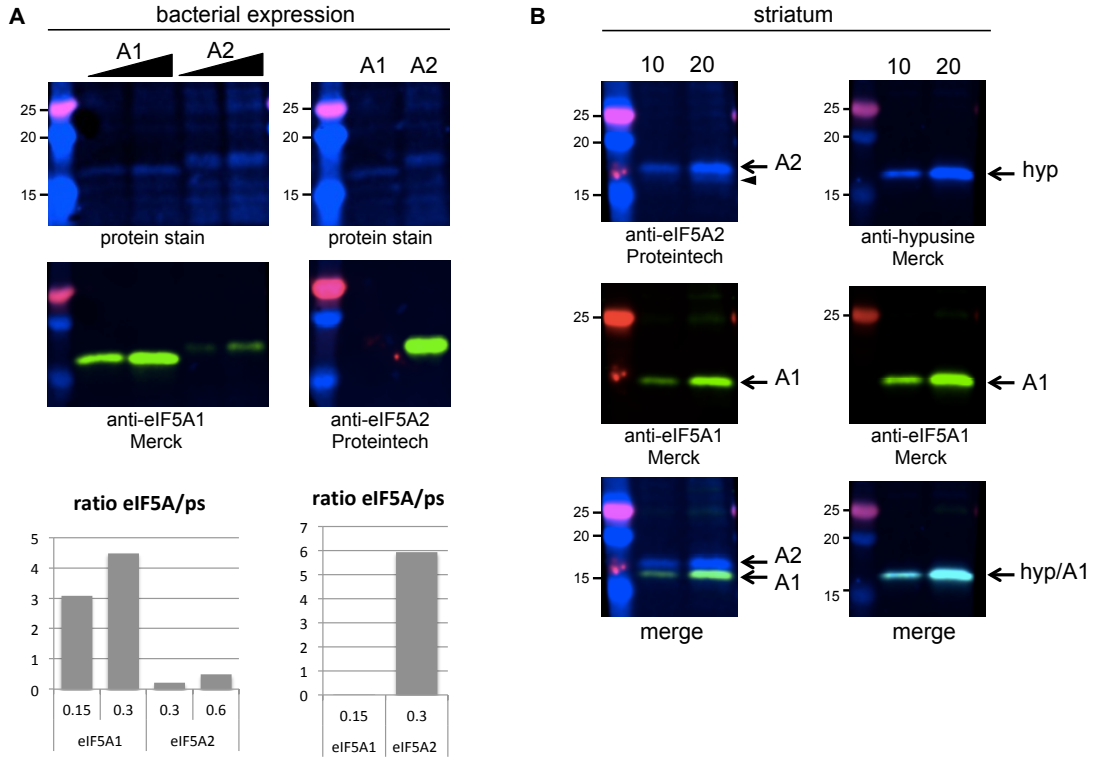

Supplementary Figure S6. Specificity test of antibodies for eIF5A1 and eIF5A2. (A) The sequences coding for human eIF5A1 and eIF5A2 were amplified from the Human MTC Panel I (#636742, Clontech) and cloned in pRSET-B vector using NdeI and EcoRI sites and overexpressed in *Escherichia coli* C41 cells. Upper panels show total protein accumulation in C41 cells transformed with the corresponding plasmid either pRSET-eIF5A1 or pRSET-eIF5A2 (Revert™ 700 Total Protein Stain, 926-11021, LI-COR). Overexpressed eIF5A1 has a higher mobility than eIF5A2. Lower panels show the incubation of the above membranes with the corresponding antibodies. The mouse monoclonal antibody raised against eIF5A1 (SAB1402762, Merck) recognizes both proteins but preferentially recognizes eIF5A1. The quantification of the relative intensity normalized by the amount of the specific protein (protein stain of the corresponding band) showed that the antibody recognizes eIF5A1 approximately 10 times better than eIF5A2. Meanwhile, the rabbit polyclonal raised against eIF5A2 (17069-1-AP, Proteintech) efficiently recognizes eIF5A2 while very poorly recognizes eIF5A1 (the band is only visible if the membrane is overexposed). The quantification of the relatively intensity normalized to the amount of each corresponding protein shows that the antibody raised against eIF5A2 recognizes eIF5A2 200 times better than eIF5A1. See graphs on the bottom panels. **(B)** We evaluated the performance of these two antibodies in mouse striatal samples. Left-upper panel shows that the antibody against eIF5A2 recognizes a band of the expected size and a shadow band of higher mobility (arrow head, likely eIF5A1). The panel below shows that the antibody

1086 raised against eIF5A1 only recognizes a band of the expected size for eIF5A1
1087 in the striatum. The merge of both channels (left-bottom panel) confirms that
1088 both proteins can be detected at the same time in the striatum and also
1089 confirms the higher mobility of eIF5A1 in striatal samples. These results also
1090 suggest, together with the quantifications made in (A) that the accumulation of
1091 eIF5A2 protein is lower than that of eIF5A1 in the striatum. On the right-upper
1092 panel we observed that the incubation of striatal samples with polyclonal anti-
1093 hypusine antibody (ABS1064-I, Merck) detects a single band and the co-
1094 incubation with mouse monoclonal antibody raised against eIF5A1
1095 (SAB1402762, Merck) confirms that this band corresponds to eIF5A1 (merge
1096 bottom panel). Thus we cannot detect hypusinated eIF5A2 in the striatum,
1097 either because eIF5A2 does not have this modification or because the amount
1098 of hypusinated eIF5A2 does not reach the detection limits for the anti-hypusine
1099 antibody.